



Quasi-two-dimensional electron gas and weak antilocalization at the interface of SrTaO₃/KTaO₃ heterostructures

Xiaoyu Zhang,¹ Zhentao Pang¹,,¹ Chenghao Yin,^{1,2} Mingyuan Yan,¹ Yang-Yang Lv,¹ Yu Deng,^{1,*} and Shan-Tao Zhang^{1,†}

¹National Laboratory of Solid State Microstructures, College of Engineering and Applied Science & Jiangsu Key Laboratory of Artificial Functional Materials & Collaborative Innovation Center of Advanced Microstructures, Nanjing University, Nanjing 210023, China

²Department of Physics, Nanjing University, Nanjing 210093, China



(Received 19 June 2023; revised 25 October 2023; accepted 13 November 2023; published 4 December 2023)

As a potential system for realizing strong spin-orbit coupling (SOC), 5d-ATaO₃ perovskite oxides have recently received extensive attention. This study presents SrTaO₃/KTaO₃ 5d-5d heterostructures with thickness-induced crossover from quasi-two-dimensional (2D) to three-dimensional (3D) transport behaviors. The sheet carrier concentration and carrier mobility of the system depend on the SrTaO₃ film thickness. The highest mobility of 430 cm² V⁻¹ s⁻¹ is observed for the heterostructure with a 16-nm-thick SrTaO₃ film, which comprises coexisting 2D and 3D transport components. Weak antilocalization, anisotropic magnetoresistance, and the plane Hall effect are observed, which robustly confirm the existence of strong SOC in the heterostructure. The tunable transport and strong correlation effect make the SrTaO₃/KTaO₃ heterostructure not only a suitable platform for investigating basic physical phenomena but also a potential material candidate for future spin devices.

DOI: [10.1103/PhysRevB.108.235114](https://doi.org/10.1103/PhysRevB.108.235114)

I. INTRODUCTION

Oxides have abundant physical properties, such as ferroelectricity, ferromagnetism, superconductivity, and magnetoresistance (MR). The combination of these physical properties with spin-orbit coupling (SOC) yields rich phenomena, providing unique methods for designing future spintronic devices [1]. As a typical example, low-dimensional oxide electronics have been proposed since the discovery of two-dimensional (2D) electron gas (EG) with high mobility at the LaAlO₃/SrTiO₃ interface [2,3]. In low-dimensional oxide electronics, the SrTiO₃-based interface has always been dominantly focused on, and heterostructures with SrTiO₃ substrates, such as LaAlO₃/SrTiO₃, LaVO₃/SrTiO₃, CaZrO₃/SrTiO₃, GdTlO₃/SrTiO₃, and CaHfO₃/SrTiO₃, have been extensively researched [2,4–7]. However, a major limitation is that the SOC strength of SrTiO₃ is not strong enough. To optimize or realize novel functional properties of the oxide heterostructure, alternative oxides with a strong SOC effect need to be found.

Basically, the Zeeman interaction between the electron spin and effective magnetic field is equivalent to the coupling between the electron spin and momentum degrees of freedom, which is called SOC [8]. SOC, which can be artificially tuned without an external magnetic field, provides a method for controlling the spin by linking the orbital motion with the electron spin [9–11]. Since the SOC magnitude is proportional to the fourth power of the number of nuclear charges, the element with a larger atomic number usually has a stronger SOC [12]. Therefore, some 5d-based

heterostructures have been investigated to illustrate unusual physical properties. For instance, the transition from a half metal to an insulator and a long-range magnetic orderly phenomenon can be realized in 5d oxide SrIrO₃ by intercalation with 3d oxide SrTiO₃ [13]. Moreover, the anomalous Hall effect, which is caused by interface ferromagnetism, is observed in the 4d-5d oxide superlattice of SrMnO₃/SrIrO₃, where SOC also plays an important role [14]. Thus, it is reasonable to expect that stronger SOC and some interesting physical phenomena may be afforded in the 5d-5d oxide heterostructure.

ATaO₃ is a type of 5d perovskite oxide. Among them, KTaO₃ (KTO) has a considerably high spin-band splitting (~ 400 meV) stemming from the 5d Ta element [9]. Thus, KTO is considered a potential material candidate for future oxide spintronics and has been drawing increasing attention. Owing to the ultrahigh mobility charge carriers and superconductivity at the KTO-based interface, KTO has become a research hotspot [1,15]. KTO is an insulating material because Ta⁵⁺ cannot contribute carriers. Therefore, research on the transport characteristics of KTO has always focused on 2DEG, which occurs on the KTO surface. However, if the Ta cation forms a stable +4 valence, the metallicity can enable the study of the intrinsic transport characteristics of the Ta-based film. Moreover, the K in KTO easily volatilizes at high temperatures, indicating that it is relatively not conducive to the growth of stoichiometric KTO thin films [16]. Hence, to suppress the volatility shortcoming of KTO and exploit the advantages of the 5d perovskite ATaO₃, one method is to introduce another 5d perovskite oxide ATa⁴⁺O₃ without volatile elements and fabricate the thin film on the bulk single crystal KTO substrate. Consequently, 5d-5d Ta-based heterostructures can be constructed to effectively enable the strong SOC of Ta.

*Corresponding author: dengyu@nju.edu.cn

†Corresponding author: stzhang@nju.edu.cn

Similar to K, alkali metal elements of Li and Na are volatile at high temperatures, and their stable valence state is +1. Therefore, the nonvolatile Sr element with a stable valence state of +2 is obviously more suitable for selection as A to obtain a conductive Ta-based $\text{Sr}^{2+}\text{Ta}^{4+}\text{O}_3$. Accordingly, the SrTaO_3 (STO)/KTO heterostructure was identified as the research object of this study. A few studies have demonstrated the existence of 2DEG at the STO/SrTiO₃ interface, but they have not observed the SOC effect [17], which may be due to the low spin-band splitting of SrTiO₃ (~ 17 meV) [9]. This study investigates the crystal structure and valence state of Ta in high-quality STO/KTO heterostructures. Moreover, by carefully tuning the ratio of three-dimensional (3D) transport in the film and quasi-2D transport at the interface, a critical heterostructure with high mobility is obtained, and a strong SOC effect is observed at the interface, which results in weak antilocalization (WAL) and a plane Hall effect (PHE).

II. EXPERIMENTAL DETAILS

Target preparation and film fabrication. STO ceramic targets were synthesized via a solid-state reaction method. Chemical stoichiometric SrCO_3 (99%) and Ta_2O_5 (99.99%) were weighed and ball milled for 24 h with ethanol as the solvent. After drying at 80 °C, the uniformly mixed powder was calcined at 1200 °C for 2 h in a crucible with a heating rate of 4 °C/min. The resultant was pressed into a cylinder and sintered at 1200 °C for 5 h with a heating rate of 4 °C/min and then naturally cooled to room temperature. (001) KTO single crystals were used as the substrate. A KrF excimer laser with a wavelength of 248 nm, a frequency of 3 Hz, and an energy density of 1.2 J/cm² was used for film deposition. During the film fabrication, the substrate temperature and flowing oxygen pressure were kept constant at 600 °C and 5×10^{-6} mbar, respectively. STO/KTO heterostructures with STO film thicknesses of 28, 22, 16, 10, and 6 nm were symbolized as samples A, B, C, D, and E, respectively.

Sample characterization. The crystal structure of the films was characterized by x-ray diffraction (XRD, Bruker D8 Discover diffractometer) with Cu $K\alpha$ radiation ($\lambda = 1.54$ Å). Aberration-corrected scanning transmission electron microscopy/electron energy loss spectroscopy (STEM/EELS) analysis was performed using field-emission TEM (Titan Cubed G2 60–300) at an accelerating voltage of 300 kV with the Ultrafast Gatan Dual-EELS system. Aberration-corrected STEM images were obtained using a high angle annular dark field (HAADF) detector, and the element distributions were confirmed via atomic resolved energy dispersive spectroscopy (EDS). The transport measurements were performed with a Quantum Design physical property measurement system (PPMS-9 T). The Ohmic contacts were made through ultrasonic aluminium-wire bonding. In usual Hall and resistance measurements, we employ the van der Pauw geometry wiring technique. The current source and voltmeter are connected to the four corners of the substrate using aluminium wires. Subsequently, this configuration enables the determination of $\rho_{2D} = \frac{\pi}{\ln 2} \frac{V_{xx}}{I_{xx}}$ and $\rho_{3D} = \rho_{2D}t$. The variable t represents the thickness of the film.

III. RESULTS AND DISCUSSION

Herein, STO thin films with various thicknesses were successfully fabricated on KTO (001) single crystal substrates. Figure S1(a) of the Supplemental Material [18] depicts the typical XRD θ -2 θ patterns of all samples; the film peak is asymmetrical and near the substrate peak overall. The reciprocal space maps of the (103) reflections for all samples in Figs. S1(b)–S1(f) do not exhibit clear differentiation between the KTO peaks and the STO peaks [18], necessitating further reliance on HAADF-STEM imaging for analyzing the lattice constant and stress effects on the film. Figure 1(a) displays a low-resolution cross-sectional HAADF-STEM image of sample C. Clearly, a sharp interface exists between the film and substrate. The STEM-EDS elemental maps illustrated in Figs. 1(b) and 1(c) show that both Sr and K are homogeneously distributed, but an interface exists between Sr and K without element diffusion across the interface. Simultaneously, Ta is homogeneously distributed across the film and substrate. The EDS maps robustly reaffirm the sharp STO/KTO interface. Moreover, Fig. 1(d) displays the high-resolution STEM-HAADF image taken near the STO/KTO interface, demonstrating the atomic-scale sharp interface and verifying the epitaxial growth of the STO films on the KTO substrate. The a/b lattice constant of STO, as measured by HAADF-STEM, is determined to be 4.070 Å, while the lattice constant c is found to be 4.073 Å. The in-plane lattice constant a/b closely approximates the out-of-plane lattice constant c , indicating a near-cubic phase and resulting in minimal interface stress.

Since Ta cations can have variable valence states, which significantly impact the heterostructure properties, the valence state of Ta in the STO/KTO heterostructures needs to be verified. Low-energy EELS spectra were measured on the film and substrate in the selected box areas indicated in Fig. 1(a); the experimental results and fitting are presented in Fig. 1(e). A major peak centered at approximately 21.3 eV, as indicated by a green arrow, was observed for both STO and KTO. This peak corresponds to the bulk plasma excitation of Ta metal and indicates a low concentration of the Ta metal state, which may be related to low oxygen pressure during film deposition [25]. The 8.0- and 29.6-eV loss peaks, denoted by red arrows, are the characteristic peaks of Ta^{5+} , and the 15.6- and 25.7-eV loss peaks, denoted by blue arrows, are the characteristic peaks of Ta^{4+} [25]. The 8.0-eV loss peak was observed in the pattern of the KTO substrate but not that of the STO film, while the 25.7-eV loss peak was observed in the pattern of the STO film but not that of the KTO substrate. If Ta^{5+} is dominant in the STO film, the crystal structure will preferably be pyrochlore $\text{Sr}_2\text{Ta}_2\text{O}_7$, which has a different crystal structure than perovskite STO and KTO; thus, the observed atomic-scale sharp interface is difficult to form. Hence, it is safe to conclude that Ta^{4+} exists in the STO film.

By employing first principles calculations, we provide further evidence for the presence of 2DEG at the interface [18]. The crystal structure model at the interface is depicted in Fig. S1(g) of the Supplemental Material [18], while the corresponding band structure is illustrated in Fig. S1(h). Notably, band (solid red line) induced by the Ta of the surface of KTO intersects with the Fermi level and contributes carriers throughout the entire model [18]. Detailed computational

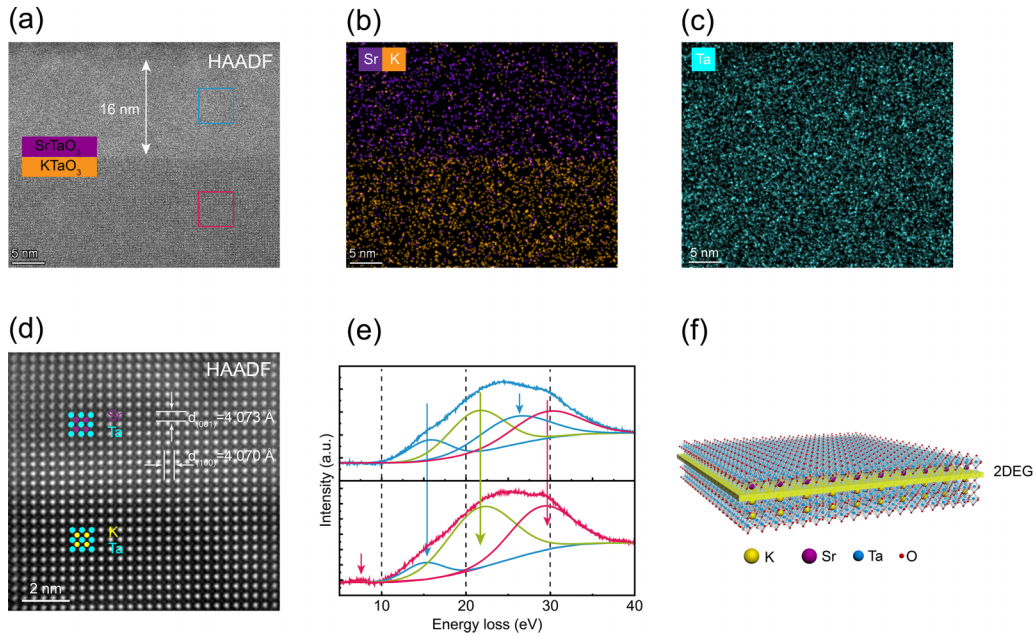


FIG. 1. Typical microstructure of the STO/KTO heterostructure. (a) Cross-sectional HAADF-STEM image of the STO/KTO heterostructure. (b), (c) STEM-EDS elemental maps of Sr-K (purple), K-K (orange), and Ta-K (blue) edges. (d) Atomic-resolution image taken near the interface of the STO/KTO heterostructure. (e) Low-energy EELS spectra taken at the box area of KTO (red) and STO (blue) shown in (a). (f) Schematic of the STO/KTO heterostructure structure and the interfacial 2DEG.

methodology can be found in the Supplemental Material [18]. Based on the above atomic-scale valence state analysis and first principles calculations, the schematic and interfacial 2DEG of the STO/KTO heterostructure are shown in Fig. 1(f). The electrons clustered in the Ta 5d orbitals significantly impact the interfacial 2D transport performance of the heterostructure.

To gain insight into the physical properties of the STO/KTO heterostructures, transport measurements were performed as functions of temperature. The temperature dependence of the 2D resistivity (ρ_{2D} - T) and 3D resistivity (ρ_{3D} - T) of the STO/KTO heterostructures is shown in Figs. 2(a) and 2(b), respectively. In general, all heterostructures exhibited metallic behavior as the resistivity increased with temperature. Two important features need to be discussed. First, if the carriers are concentrated at the interface, the thickness dependence of ρ_{2D} at low temperatures exhibits a narrow range, and an increasing trend in ρ_{3D} would be anticipated with increasing STO film thickness [1]. Nevertheless, there is a significant variation (~ 2.5 orders of magnitude) in the ρ_{2D} value, and ρ_{3D} decreases as the film thickness increases. This evidence indicates that the conducting channel is not limited to only the STO/KTO interface, i.e., the STO film contributes to the resistivity, which is self-consistent with the thickness-dependent resistivity. In our opinion, the conduction of the STO film stems from its dominant +4 chemical valence state, wherein the STO band structure has a zero energy gap [26].

The low-temperature graph of ρ/ρ_{2K} [Fig. 2(c)] clearly illustrates the contrasting trends in resistivity upturn among samples with different thicknesses. It is evident that the sample A does not exhibit a resistivity upturn at low temperatures, whereas the thinner samples (less than 28 nm) show a

pronounced resistivity upturn. For sample A, the ρ_{3D} - T curve at the temperature range 2–25 K can be well fitted by the following equation [Fig. S2(a)] [18]:

$$\rho_{3D} = \rho_0 + BT^3, \quad (1)$$

in which ρ_0 is the residual resistivity and the second term is the contribution of electron-phonon (e -ph) interactions [27]; the fitting result is shown in Fig. S2(a) [18]. However, for thinner samples (below 28 nm), factors contributing to resistivity upturn at low temperatures need to be considered, such as electron-electron (e - e) interaction, weak localization (WL), and the Kondo effect [28–30]. Magnetization hysteresis (M - H) measurements were conducted on 22-nm samples at various temperatures [Fig. S2(b)] [18]. The weak and temperature independent magnetism suggest that the oxygen vacancies within the substrate and film are responsible for the source of magnetism in measurement, rather than the film itself. The ρ_{3D} - T curves of sample E under various applied magnetic fields at low temperature are presented in Fig. S2(c) [18], demonstrating that resistivity upturn is not suppressed by magnetic fields at low temperatures. Therefore, both the WL and Kondo effect can be excluded, leaving only the electron-electron (e - e) interaction to be considered [29]. In a 3D system, the e - e interaction exhibits a power law dependence on temperature, while in a 2D system, it shows a logarithmic dependence on temperature [28]. Hence, Eq. (2) can be well fitted [Fig. S2(a)] [18]:

$$\rho_{3D} = \rho_0 + BT^3 - C\ln(T) - DT^{\frac{1}{2}}, \quad (2)$$

where ρ_0 represents the residual resistivity, the second term accounts for e -ph interactions contribution, the third term describes 2D e - e interactions, and the fourth term represents

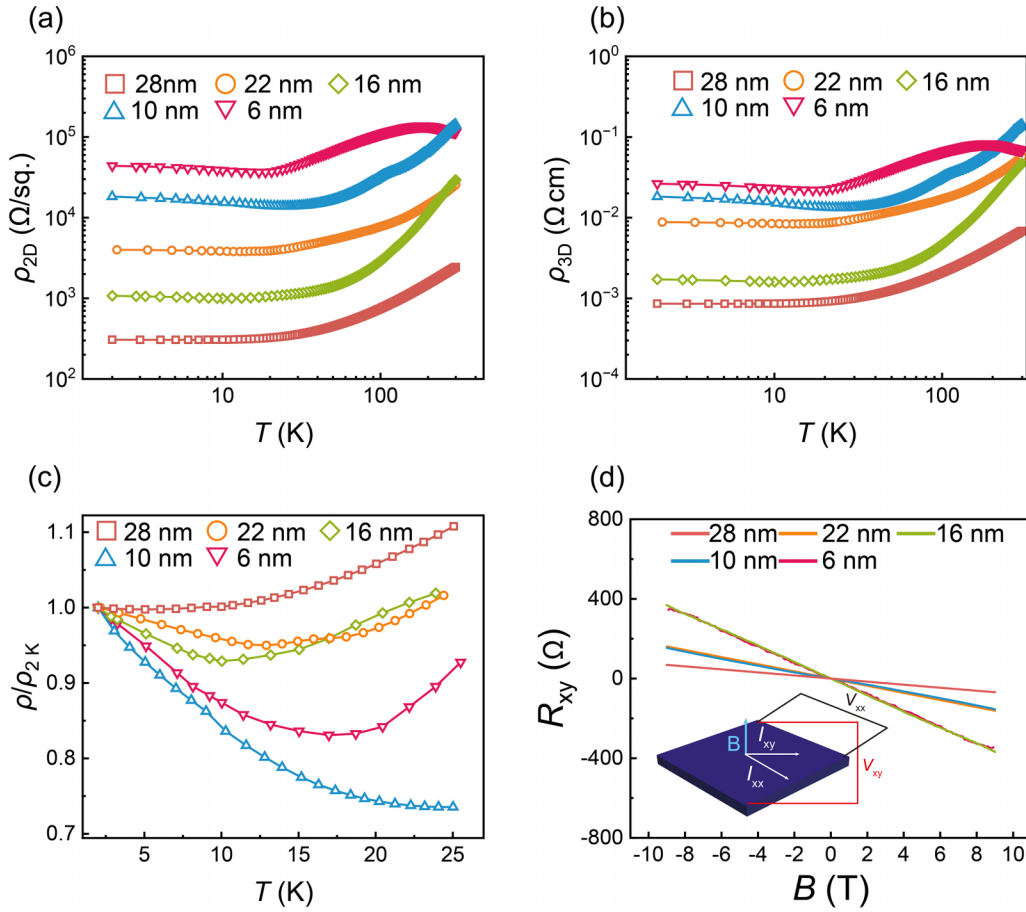


FIG. 2. Temperature-dependent (a) 2D and (b) 3D resistivities of the STO/KTO heterostructures. (c) Temperature-dependent ρ/ρ_{2K} curves. (d) Hall resistance of all samples measured at 2 K. The inset in (d) shows the direction of the current and applied out-of-plane magnetic field during the Hall effect and MR measurement.

3D e - e interactions. The good fitting of Eq. (2) [derived by incorporating 2D electron-electron (e - e) and 3D e - e terms into Eq. (1)] suggests the presence of 2D transport and 3D transport in samples B and C, leading to a quasi-two-dimensional transport outcome. Further thinning samples (D and E) may lead to poor fitting in Fig. S2(a) [18] due to increased influence from interface SOC.

To determine the characteristics of the carriers and carrier density of the STO/KTO heterostructures, the Hall effect of the heterostructures with various STO thicknesses was measured at 2 K [Fig. 2(d)]. R_{xy} can be modified with $R_{xy} = \frac{1}{2}[R'_{xy}(B) - R'_{xy}(-B)]$, where $R'_{xy}(B)$ is the signal obtained by experimental measurement. The calculated 2D Hall coefficient (R_H^{2D}) is displayed in Fig. S2(d) [18]. The negative slopes of the R_{xy} - B curves denote that electron dominate the electrical transport process. Interestingly, R_H^{2D} is nonmonotonically dependent on the STO thickness, and sample C had a maximum R_H^{2D} of $41 \Omega T^{-1}$. To explain this nonmonotonous trend of R_H^{2D} and determine the transport mechanism, the temperature-dependent sheet charge carrier density (n_s) and mobility (μ) of all heterostructures are calculated and plotted in Fig. 3.

Figure 3(a) shows that the n_s value of the heterostructures depends on the STO thickness. The n_s value for the STO film thickness of 28 nm exhibited a clear temperature

dependence, decreasing from $1.9 \times 10^{14} \text{ cm}^{-2}$ at 300 K to $8.2 \times 10^{13} \text{ cm}^{-2}$ at 2 K, thereby confirming that the dominant transport mechanism originates from bulk carriers. Furthermore, the n_s value of the heterostructure with a 28-nm-thick STO film was significantly higher compared to other heterostructures due to an overestimation caused by underestimating the R_H^{2D} value of the interface channel. In contrast, for heterostructures with STO film thicknesses ≤ 22 nm, the n_s value showed only weak temperature dependence, indicating that interfacial two-dimensional (2D) transport mechanism prevails [31]. This observation indicates that two transport channels exist in the STO/KTO heterostructures. As the film thickness decreases, the presence of bulk carriers in the film becomes less pronounced, leading to a quasi-2D transport regime. Such a heterostructure may have a maximum μ . As shown in Fig. 3(b), a maximum μ of $430 \text{ cm}^2 \text{ V}^{-1} \text{ s}^{-1}$ was observed for sample C with a 16-nm-thick STO film, for which μ can even be $17 \text{ cm}^2 \text{ V}^{-1} \text{ s}^{-1}$ at room temperature, which is higher than that of most SrTiO_3 -based 2DEG at room temperature [2,4,5].

Figures 4(a)–4(c) display the typical temperature-dependent MR of the heterostructures with varying STO thickness as a function of the applied magnetic field (B), where $\text{MR}(\%) = \frac{R_{xx}(B) - R_{xx}(0)}{R_{xx}(0)} \times 100\%$. R_{xx} can be modified with $R_{xx} = \frac{1}{2}[R'_{xx}(B) + R'_{xx}(-B)]$, where $R'_{xx}(B)$ is the

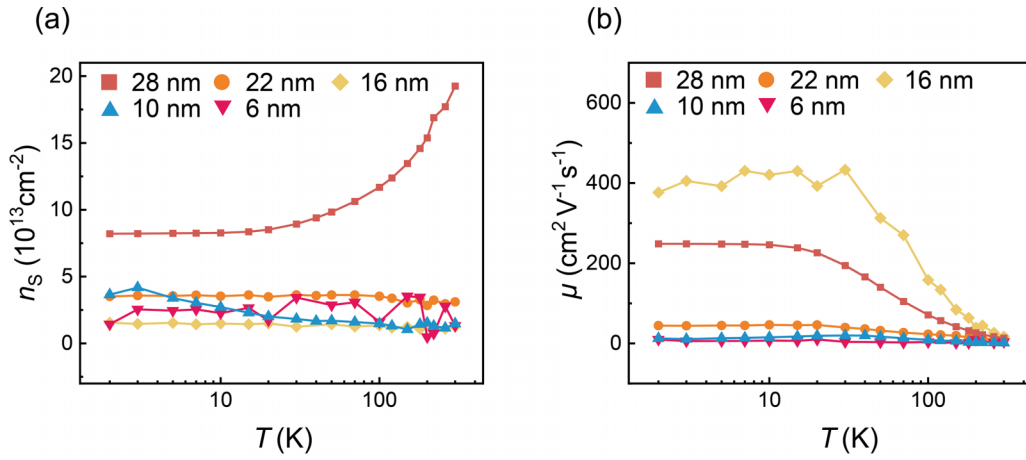


FIG. 3. Temperature-dependent (a) sheet charge carrier density (n_s) and (b) carrier mobility (μ) of the STO/KTO heterostructures.

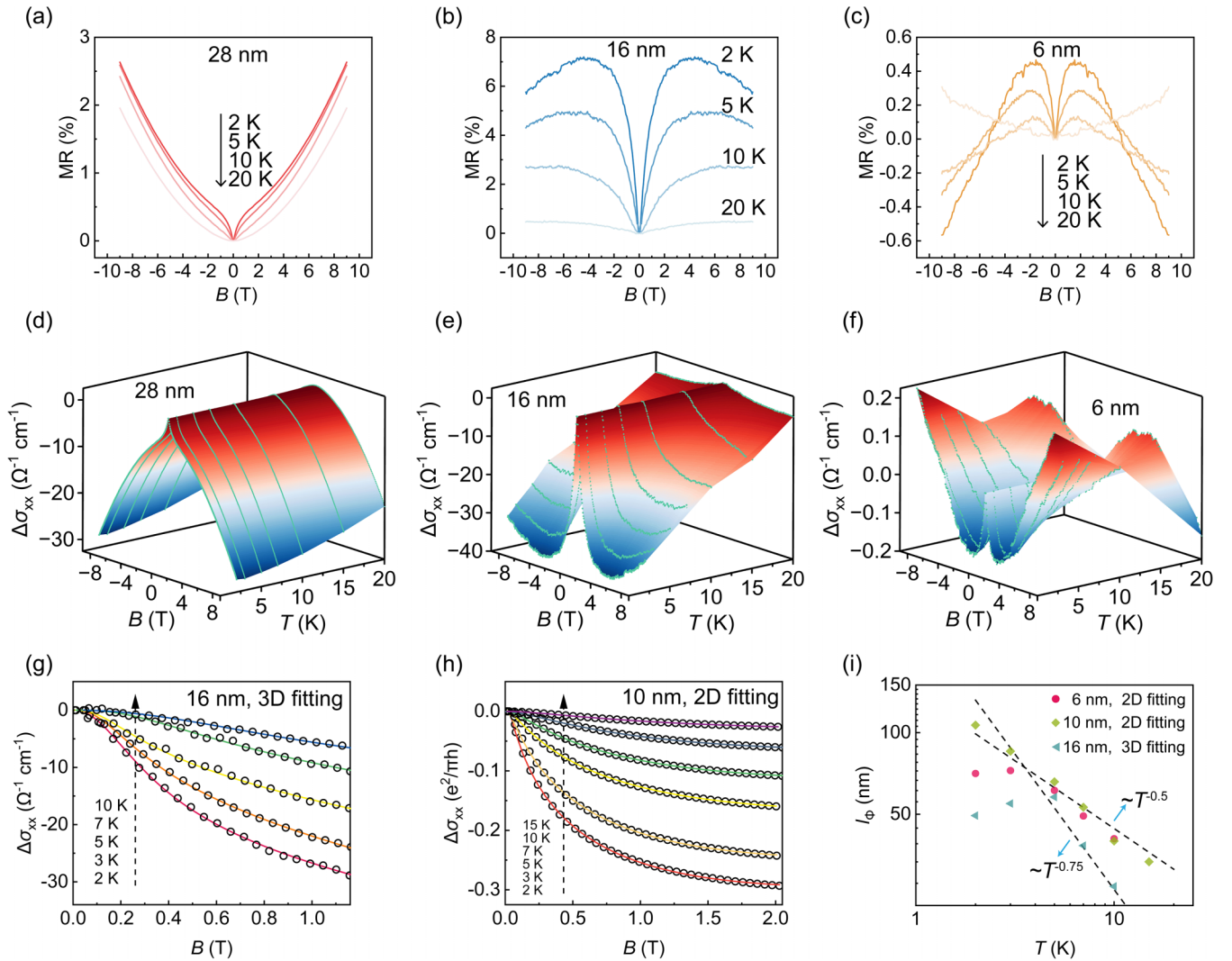


FIG. 4. (a)–(c) Typical temperature-dependent magnetoresistance–magnetic field (MR-B) curves of samples A, C, and E. (d)–(f) Temperature-dependent weak antilocalization (WAL) within the temperature range of 2–20 K of samples A, C, and E. (g) Measured magnetoconductance (MC) of sample C and fitting result based on the 3D WAL formula. (h) MC of sample E and fitting result based on the 2D Hikami-Larkin-Nagaoka formula. (i) Dependence of phase coherence length (l_ϕ) on temperature for samples C, D, and E.

signal obtained by experimental measurement under varying magnetic fields. Sharp resistance cusps were observed at low B and low T for all the heterostructures, which is a typical sign of WAL stemming from the SOC [27,32]. Comparison of the MR- B curves of samples A, C, and E shows that for sample A, the WAL intensity at $B > 2$ T was weak because its WAL width, which is characterized by the magnetic field value corresponding to the cusps [33], was narrower than that for samples C and E. With increasing magnetic field ($B > 2$ T), MR tends to dispose of the WAL influence and becomes positively correlated with B^2 due to classical orbital effects dominated by the Lorentz force. However, for samples C and E, which have comparatively thinner STO films, the SOC intensity gradually increased with the WAL width. This is because the 2D interfacial transport became dominant. Simultaneously, the MR above 2 T was not positively correlated with B . A negative MR (-0.6%) existed for sample E, as the strong SOC affected the 2DEG transport channel at the interface [34]. To better visualize the WAL phenomenon afforded by the SOC, the applied-magnetic-field-dependent magnetoconductance (MC) $\Delta\sigma_{xx}$ of samples A, C, and E at 2–20 K is plotted in Figs. 4(d)–4(f), and the $\Delta\sigma_{xx}$ of samples B and D at 2–20 K is plotted in Fig. S3 [18]. The general evolution of the $\Delta\sigma_{xx}$ - B curves signifies the thickness dependence of WAL.

To understand the relation between the transport mechanism and the STO film thickness (Fig. 3), the relationship between $\Delta\sigma_{xx}$ and the applied magnetic field was analyzed. The cusp of sample C below 1.6 T can be well fitted by the following simplified 3D WAL formula [35]:

$$\Delta\sigma_{xx}(B) = C_{\text{WAL}} \left(\sqrt{B} \frac{B^2}{B^2 + B_c^2} + \gamma B^2 \frac{B_c^2}{B^2 + B_c^2} \right), \quad (3)$$

where C_{WAL} is the antilocalization coefficient reflecting the strength of the localization degree. Additionally, $B_c = \hbar/e l_\varphi^2$ is the characteristic magnetic field, and l_φ is the phase coherence length. $\Delta\sigma_{xx}$ of samples B and C can be well fitted using this 3D WAL model [Fig. S4(a) [18] and Fig. 4(g), respectively], indicating the relatively preferred 3D transport mechanism, although sample C has a critical heterostructure with coexisting 3D and quasi-2D transport mechanisms, as discussed above. Moreover, this critical heterostructure of sample C yields the maximum C_{WAL} (-18.3) at 2 K, denoting its large WAL intensity [28]. When the STO thickness decreases, the transport mechanism tends to be quasi-2D. Therefore, $\Delta\sigma_{xx}$ cannot be well fitted using the above 3D WAL formula. Here, the 2D Hikami-Larkin-Nagaoka (HLN) formula is applicable [36]:

$$\Delta\sigma_{xx}(B) = -\frac{e^2}{\pi h} \left[\frac{1}{2} \Psi \left(\frac{1}{2} + \frac{B_\varphi}{B} \right) - \frac{1}{2} \ln \left(\frac{B_\varphi}{B} \right) - \Psi \left(\frac{1}{2} + \frac{B_\varphi + B_{\text{SO}}}{B} \right) + \ln \left(\frac{B_\varphi + B_{\text{SO}}}{B} \right) - \frac{1}{2} \Psi \left(\frac{1}{2} + \frac{B_\varphi + B_{\text{SO}}}{B} \right) + \frac{1}{2} \ln \left(\frac{B_\varphi + 2B_{\text{SO}}}{B} \right) \right] \quad (4)$$

where $B_\varphi = \hbar/e l_\varphi^2$, $\Psi(x)$ is the digamma function, and B_φ is the dephasing magnetic field determined by l_φ . B_{SO} is the spin-

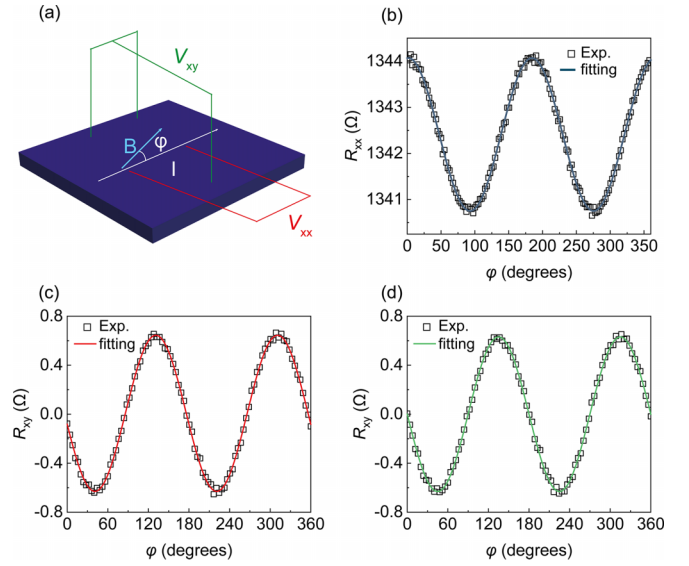


FIG. 5. (a) Schematic illustrations of the anisotropic MR and plane Hall effect measurement configurations. Angle-dependent (b) R_{xx} and (c) the average planar Hall resistance measured for sample C at 2 K and a 9 T in-plane magnetic field. (d) The intrinsic planar Hall resistance after subtracting the misalignment components.

orbit scattering field determined by the spin-orbit scattering length l_{SO} . Actually, the $\Delta\sigma_{xx}$ measured at low temperatures for samples D and E can be well fitted based on the HLN mode, as plotted in Fig. 4(h) and Fig. S4(b) [18], respectively.

Subsequently, the temperature-dependent l_φ of samples C, D, and E is obtained and shown in Fig. 4(i). l_φ exhibits an obvious temperature dependence, mainly stemming from inelastic-scattering-induced dephasing. Furthermore, l_φ can be related to T through $l_\varphi \propto T^{-P/2}$, where P is a parameter determined by the dephasing mechanism. In a 3D system, $P=1.5$ for electron-electron interactions and $P=3$ for electron-phonon interactions. In a 2D system, $P=1$ for electron-electron interactions [28,37]. The relationship between the fitted l_φ and T shows that $P=1$ for both samples D and E, indicating their quasi-2D system characteristics. In contrast, $P=1.5$ for sample C, indicating its 3D system characteristics. Accordingly, the dephasing is dominated by electron-electron interactions for these samples. At low temperatures, l_φ tends to deviate from the linear relationship, usually owing to other constant dephasing [38].

In general, anisotropic MR (AMR) and PHE are observed in magnetic materials with crystallographic anisotropy [39,40] or topological materials with Adler-Bell-Jackiw chiral anomaly and nontrivial Berry curvature [41–43]. However, it has been theoretically predicted that Rashba-Dresselhaus spin-orbit splitting may afford AMR and PHE in materials with a strong SOC effect [44–46], direct experimental observations of PHE and AMR in SOC systems are rare. To phenomenologically confirm the existence of strong SOC in our STO/KTO heterostructures, AMR and PHE were measured for sample C. The results are plotted in Fig. 5. During the measurements, the applied magnetic field was maintained in the heterostructure surface plane, as schematically shown in Fig. 5(a), and the transverse resistance R_{xy} and longitudinal

resistance R_{xx} were measured. As shown in Figs. 5(b) and 5(c), when the angle between the applied magnetic field and current was changed, both R_{xx} and R_{xy} exhibited twofold periodic oscillation. Moreover, the AMR can be fitted using the following equation [1,47]:

$$R_{xx}^{\text{planar}} = R_{xx}^{\varphi=90^\circ} + \Delta R^{\text{chiral}} \cos^2 \varphi \quad (5)$$

in which φ is the angle between the magnetic field and current, $R_{xx}^{\varphi=90^\circ}$ is the longitudinal resistance with $\varphi = 90^\circ$, and ΔR^{chiral} is the contribution of chirality to resistance. By measuring the voltage in two directions, the separation of R_{xx} and R_{xy} was achieved to a significant extent [48]. However, due to inherent disorder in the Hall structure during the wiring process, there is a minor contribution of AMR in the PHE measurement. The PHE data in Fig. 5(c) can be fitted with a small AMR ($\cos^2 \varphi$) contribution [43,49]:

$$R_{xy}^{\text{planar}} = -a \sin \varphi \cos \varphi + b \cos^2 \varphi + c. \quad (6)$$

The first part represents the inherent PHE, while the second and third parts arise from the misalignment of the Hall configuration. The results in Fig. 5(c) can be accurately fitted using formula (6), as indicated by the solid line in Fig. 5(c). By excluding the influence of the second and third parts, the intrinsic PHE is depicted in Fig. 5(d). The detailed data processing is illustrated in Fig. S5 of the Supplemental Material [18]. The well-fitted AMR and PHE further confirm

the existence of Rashba splitting owing to SOC and prove the presence of strong SOC in the STO/KTO heterostructures.

IV. CONCLUSION

In this study, high-quality STO/KTO heterostructures were fabricated and investigated. As the STO film thickness decreased, a crossover from a 3D to a quasi-2D transport mechanism was observed. Consequently, the heterostructure with a 16-nm-thick STO film comprised coexisting 3D and 2D transport components with the highest mobility of $430 \text{ cm}^2 \text{ V}^{-1} \text{ s}^{-1}$. The observation of WAL, AMR, and PHE robustly verified the strong SOC effect in the heterostructure. The tunable transport and strong correlation effect make the proposed STO/KTO heterostructure not only a platform for investigating basic physical phenomena but also a potential material candidate for future spin devices.

ACKNOWLEDGMENTS

This work was supported by the National Key R&D Program of China (Grant No. 2020YFA0711504), the National Natural Science Foundation of China (Grants No. 12174179 and No. 51721001), Natural Science Foundation of Jiangsu Province (Grants No. BK20201246 and No. BK20221251), and the Dengfeng B project of Nanjing University.

-
- [1] N. Wadehra, R. Tomar, R. M. Varma, R. Gopal, Y. Singh, S. Dattagupta, and S. Chakraverty, Planar Hall effect and anisotropic magnetoresistance in polar-polar interface of LaVO_3 - KTaO_3 with strong spin-orbit coupling, *Nat. Commun.* **11**, 874 (2020).
 - [2] A. Ohtomo and H. Hwang, A high-mobility electron gas at the LaAlO_3 / SrTiO_3 heterointerface, *Nature (London)* **427**, 423 (2004).
 - [3] Y.-Y. Pai, A. Tylan-Tyler, P. Irvin, and J. Levy, Physics of SrTiO_3 -based heterostructures and nanostructures: A review, *Rep. Prog. Phys.* **81**, 036503 (2018).
 - [4] Y. Hotta, T. Susaki, and H. Hwang, Polar discontinuity doping of the LaVO_3 / SrTiO_3 interface, *Phys. Rev. Lett.* **99**, 236805 (2007).
 - [5] L. Chen, J. Li, Y. Tang, Y.-Y. Pai, Y. Chen, N. Pryds, P. Irvin, and J. Levy, Extreme reconfigurable nanoelectronics at the CaZrO_3 / SrTiO_3 interface, *Adv. Mater.* **30**, 1801794 (2018).
 - [6] J. Betancourt, T. R. Paudel, E. Y. Tsymlal, and J. Velev, Spin-polarized two-dimensional electron gas at GdTiO_3 / SrTiO_3 interfaces: Insight from first-principles calculations, *Phys. Rev. B* **96**, 045113 (2017).
 - [7] M. Zhang, K. Du, T. Ren, H. Tian, Z. Zhang, H. Y. Hwang, and Y. Xie, A termination-insensitive and robust electron gas at the heterointerface of two complex oxides, *Nat. Commun.* **10**, 4026 (2019).
 - [8] A. Soumyanarayanan, N. Reyren, A. Fert, and C. Panagopoulos, Emergent phenomena induced by spin-orbit coupling at surfaces and interfaces, *Nature (London)* **539**, 509 (2016).
 - [9] H. Nakamura and T. Kimura, Electric field tuning of spin-orbit coupling in KTaO_3 field-effect transistors, *Phys. Rev. B* **80**, 121308(R) (2009).
 - [10] I. Žutić, J. Fabian, and S. D. Sarma, Spintronics: Fundamentals and applications, *Rev. Mod. Phys.* **76**, 323 (2004).
 - [11] D. D. Awschalom and M. E. Flatté, Challenges for semiconductor spintronics, *Nat. Phys.* **3**, 153 (2007).
 - [12] P. D. B. Collins, The theory of atomic structure and spectra, *Phys. Bull.* **33**, 243 (1982).
 - [13] J. Matsuno, K. Ihara, S. Yamamura, H. Wadati, K. Ishii, V. V. Shankar, H.-Y. Kee, and H. Takagi, Engineering a spin-orbital magnetic insulator by tailoring superlattices, *Phys. Rev. Lett.* **114**, 247209 (2015).
 - [14] J. Nichols *et al.*, Emerging magnetism and anomalous Hall effect in iridate-manganite heterostructures, *Nat. Commun.* **7**, 12721 (2016).
 - [15] Z. Chen, Y. Liu, H. Zhang, Z. Liu, H. Tian, Y. Sun, M. Zhang, Y. Zhou, J. Sun, and Y. Xie, Electric field control of superconductivity at the LaAlO_3 / KTaO_3 (111) interface, *Science* **372**, 721 (2021).
 - [16] K. Szot, W. Speier, M. Pawelczyk, J. Kwapulinski, J. Hulliger, H. Hesse, U. Breuer, and W. Quadackers, Chemical inhomogeneity in the near-surface region of KTaO_3 evolving at elevated temperatures, *J. Phys.: Condens. Matter* **12**, 4687 (2000).
 - [17] J. Zhang *et al.*, Design and realization of Ohmic and Schottky interfaces for oxide electronics, *Small Sci.* **2**, 2100087 (2022).
 - [18] See Supplemental Material at <http://link.aps.org/supplemental/10.1103/PhysRevB.108.235114> for x-ray characterization of the samples; first-principle calculation; fitting results for the low-temperature ρ_{3D} - T curves; magnetization hysteresis loops of sample B; ρ_{3D} - T curves under an applied magnetic field of sample E; two-dimensional Hall coefficient as a func-

- tion of thickness; temperature-dependent weak antilocalization phenomena of samples B and D; WAL mode fitting of magnetoresistance of samples B and E; method for measurement of planar Hall effect and anisotropic magnetoresistance and data processing procedures for planar Hall measurements (see also Refs. [19–24] therein).
- [19] P. Hohenberg and W. Kohn, Inhomogeneous electron gas, *Phys. Rev.* **136**, B864 (1964).
 - [20] W. Kohn and L. J. Sham, Self-consistent equations including exchange and correlation effects, *Phys. Rev.* **140**, A1133 (1965).
 - [21] G. Kresse and J. Hafner, *Ab initio* molecular-dynamics simulation of the liquid-metal–amorphous-semiconductor transition in germanium, *Phys. Rev. B* **49**, 14251 (1994).
 - [22] G. Kresse and J. Furthmüller, Efficient iterative schemes for *ab initio* total-energy calculations using a plane-wave basis set, *Phys. Rev. B* **54**, 11169 (1996).
 - [23] J. P. Perdew, K. Burke, and M. Ernzerhof, Generalized gradient approximation made simple, *Phys. Rev. Lett.* **77**, 3865 (1996).
 - [24] H. J. Monkhorst and J. D. Pack, Special points for Brillouin-zone integrations, *Phys. Rev. B* **13**, 5188 (1976).
 - [25] G.-S. Park *et al.*, *In situ* observation of filamentary conducting channels in an asymmetric Ta₂O_{5-x}/TaO_{2-x} bilayer structure, *Nat. Commun.* **4**, 2382 (2013).
 - [26] Z. Liu, H. Liu, J. Ma, X. Wang, G. Li, and H. Chen, Emergent topological states via digital (001) oxide superlattices, *Npj Comput. Mater.* **8**, 208 (2022).
 - [27] H. Liu *et al.*, Quasi-2D transport and weak antilocalization effect in few-layered VSe₂, *Nano Lett.* **19**, 4551 (2019).
 - [28] P. A. Lee and T. Ramakrishnan, Disordered electronic systems, *Rev. Mod. Phys.* **57**, 287 (1985).
 - [29] G. Bergmann, Weak localization in thin films: A time-of-flight experiment with conduction electrons, *Phys. Rep.* **107**, 1 (1984).
 - [30] A. Brinkman, M. Huijben, M. van Zalk, J. Huijben, U. Zeitler, J. C. Maan, W. G. van der Wiel, G. Rijnders, D. H. A. Blank, and H. Hilgenkamp, Magnetic effects at the interface between non-magnetic oxides, *Nat. Mater.* **6**, 493 (2007).
 - [31] Z. Dziuba, J. Antoszewski, J. M. Dell, L. Faraone, P. Kozodoy, S. Keller, B. Keller, S. P. DenBaars, and U. K. Mishra, Magnetic field dependent Hall data analysis of electron transport in modulation-doped AlGaIn/GaN heterostructures, *J. Appl. Phys.* **82**, 2996 (1997).
 - [32] H. Li, H.-W. Wang, Y. Li, H. Zhang, S. Zhang, X.-C. Pan, B. Jia, F. Song, and J. Wang, Quantitative analysis of weak antilocalization effect of topological surface states in topological insulator BiSbTeSe₂, *Nano Lett.* **19**, 2450 (2019).
 - [33] Y. Zhang, F. Xue, C. Tang, J. Li, L. Liao, L. Li, X. Liu, Y. Yang, C. Song, and X. Kou, Highly efficient electric-field control of giant Rashba spin–orbit coupling in lattice matched InSb/CdTe heterostructures, *ACS Nano* **14**, 17396 (2020).
 - [34] A. Caviglia, M. Gabay, S. Gariglio, N. Reyren, C. Cancellieri, and J.-M. Triscone, Tunable Rashba spin-orbit interaction at oxide interfaces, *Phys. Rev. Lett.* **104**, 126803 (2010).
 - [35] C.-L. Zhang *et al.*, Signatures of the Adler–Bell–Jackiw chiral anomaly in a Weyl fermion semimetal, *Nat. Commun.* **7**, 10735 (2016).
 - [36] S. Hikami, A. I. Larkin, and Y. Nagaoka, Spin-orbit interaction and magnetoresistance in the two dimensional random system, *Prog. Theor. Phys.* **63**, 707 (1980).
 - [37] D. Thouless, Maximum metallic resistance in thin wires, *Phys. Rev. Lett.* **39**, 1167 (1977).
 - [38] J.-J. Lin and J. Bird, Recent experimental studies of electron dephasing in metal and semiconductor mesoscopic structures, *J. Phys.: Condens. Matter* **14**, R501 (2002).
 - [39] V. D. Ky, Planar Hall effect in ferromagnetic films, *Phys. Status Solidi* **26**, 565 (1968).
 - [40] S. T. Gönnenwein, R. S. Keizer, S. W. Schink, I. Van Dijk, T. M. Klapwijk, G.-X. Miao, G. Xiao, and A. Gupta, Planar Hall effect and magnetic anisotropy in epitaxially strained chromium dioxide thin films, *Appl. Phys. Lett.* **90**, 142509 (2007).
 - [41] A. Taskin, H. F. Legg, F. Yang, S. Sasaki, Y. Kanai, K. Matsumoto, A. Rosch, and Y. Ando, Planar Hall effect from the surface of topological insulators, *Nat. Commun.* **8**, 1340 (2017).
 - [42] R. Singha, S. Roy, A. Pariari, B. Satpati, and P. Mandal, Planar Hall effect in the type-II Dirac semimetal VAl₃, *Phys. Rev. B* **98**, 081103(R) (2018).
 - [43] S. Nandy, G. Sharma, A. Taraphder, and S. Tewari, Chiral anomaly as the origin of the planar Hall effect in Weyl semimetals, *Phys. Rev. Lett.* **119**, 176804 (2017).
 - [44] M. Trushin, K. Výborný, P. Morawski, A. A. Kovalev, J. Schliemann, and T. Jungwirth, Anisotropic magnetoresistance of spin-orbit coupled carriers scattered from polarized magnetic impurities, *Phys. Rev. B* **80**, 134405 (2009).
 - [45] P. Li, C. Zhang, Y. Wen, L. Cheng, G. Nichols, D. G. Cory, G.-X. Miao, and X.-X. Zhang, Anisotropic planar Hall effect in the type-II topological Weyl semimetal WTe₂, *Phys. Rev. B* **100**, 205128 (2019).
 - [46] N. Kumar, S. N. Guin, C. Felser, and C. Shekhar, Planar Hall effect in the Weyl semimetal GdPtBi, *Phys. Rev. B* **98**, 041103(R) (2018).
 - [47] P. Li, C. H. Zhang, J. W. Zhang, Y. Wen, and X. X. Zhang, Giant planar Hall effect in the Dirac semimetal ZrTe_{5-δ}, *Phys. Rev. B* **98**, 121108(R) (2018).
 - [48] F. C. Chen *et al.*, Planar Hall effect in the type-II Weyl semimetal T_d-MoTe₂, *Phys. Rev. B* **98**, 041114(R) (2018).
 - [49] A. A. Burkov, Giant planar Hall effect in topological metals, *Phys. Rev. B* **96**, 041110(R) (2017).